Desalination and Water Treatment
www.deswater.com
doi: 10.1080/19443994.2015.1046142

57 (2016) 11699–11711
May

Taylor & Francis
Taylor & Francis Group

Parametric distributions of a horizontal-tube falling film evaporator for desalination

Luyuan Gong, Shengqiang Shen*, Hua Liu, Xingsen Mu

Key Laboratory of Liaoning Province for Desalination, Dalian University of Technology, Dalian 116024, Liaoning, China, Tel. +86 13624081667; email: dutgly@yahoo.com (L. Gong), Tel. +86 411 84708464; Fax: +86 411 84707963; email: zzbshen@dlut.edu.cn (S. Shen), Tel. +86 13889606832; email: liuhua@mail.dlut.edu.cn (H. Liu), Tel. +86 13591366001; email: magicruby@gmail.com (X. Mu)

Received 10 July 2014; Accepted 23 April 2015

ABSTRACT

Three independent experiments which correspond to the characteristic study on the performance of the horizontal-tube falling film evaporators were carried out, and each came out with a validated model for its performance prediction. A comprehensive distributed parameter model was developed based on the above three models to simulate a large tube bundle consisting of 160 rows and 80 columns aluminum-brass tubes in a horizontal-tube falling film evaporator. The simulation was conducted with the superficial evaporation temperature on the shell side of 60˚C, the superficial overall temperature difference of 3.0˚C, the inlet brine salinity of 30 g/kg, the inlet brine spray density of 0.06 kg/m s, and the maximum steam inlet velocity of 40 m/s. The non-uniform distributions of several thermal parameters are presented and discussed.

Keywords: Falling film evaporator; Horizontal-tube bundle; Distributed parameter model; Distributions of parameters

1. Introduction

Falling film evaporators have many advantages over flooded evaporators: higher heat transfer coefficient, minimal pressure drop, operation under small temperature difference, etc. and have wide applications in desalination, refrigeration, food industry, and other areas. Numerous experiments have been carried out on a single horizontal tube to study the performance of the outside-tube falling film evaporation or the inside-tube condensation. For falling film evaporation outside a horizontal tube, generally the liquid flow rate, the evaporation temperature, the heat flux, and the tube space are considered as the main parameters that influence the evaporation heat transfer coefficient [1–3]. Distributions of the local heat transfer coefficients along the tube peripheral direction were demonstrated through experimental studies or theoretical analysis [4,5]. For the condensation heat transfer inside a horizontal tube, previous scholars have carried out investigation on the flow pattern or the heat transfer performance based on the flow patterns inside circular tubes [6–8]. Among the various steam flow patterns inside the circular tubes, the stratified flow pattern [9–11] is commonly studied for the application in MED systems considering the relatively lager tube inside diameter and smaller steam inlet velocity applied in the systems.

---

*Corresponding author.

Falling film evaporation on a tube bundle, compared with a single tube, shows complexities because of the liquid splash or intertube evaporation. Xu [12] investigated the falling film evaporation performance on a horizontal-tube bundle and discussed the interaction between the shell-side parameters and the tube-side parameters. Liu et al. [13] found within a tube bundle, brine salinity has little influence on the evaporation heat transfer. Fujita and Tsutsui [14] presented correlations for the prediction of local dryout outside tube surfaces and its influence on the heat transfer performance. Yang and Wang [15] used distribution parameter model to simulate the heat transfer performance with different tube pass arrangements in large falling film evaporators. Hou et al. [16,17] adopted the same method to study the heat and mass transfer performance along the tube bundle row and length direction in horizontal falling film evaporators.

Despite many experimental and analytical works on the heat transfer performance of a tube bundle, few studies have investigated the tube bundle effects caused by the intertube vapor flow resistance or the heat transfer performance using the nature seawater as the operating liquid. In this paper, a distributed parameter model is established based on three related experiments. The evaporation heat transfer coefficient was obtained with the nature seawater as the operating liquid. The distributions of several thermal parameters along the tube row, tube column, and tube length directions were discussed within the evaporator.

2. Experimental apparatus and methods

Three experiments were carried out for the study of falling film evaporation outside a single tube, the condensation inside a single tube, and the steam flow resistance on the shell side of a falling-film tube evaporator as shown from Figs. 1 to 3.

2.1. Experiment 1: Falling film evaporation outside a single tube

The objective of this experiment is to obtain the evaporation heat transfer coefficient outside a horizontal aluminum-brass tube. The system includes a heating tank, an evaporator, a condenser, in addition to a liquid feeder, and a metering pot as shown in Fig. 1. The brine starts from the heating tank where the temperature of the liquid is controlled to the required values, and then the brine is pumped up to the liquid feeder followed by several regulation valves and a flow meter. From the liquid feeder, the fluid is supplied at the desired flow rate to the testing cell forming falling films outside horizontal tubes as it continuously flows down. Part of the brine evaporates outside the heating tube. The vapor condenses in the condenser to keep a steady pressure of the cell. The rest brine is pumped into the heating tank for recycling.

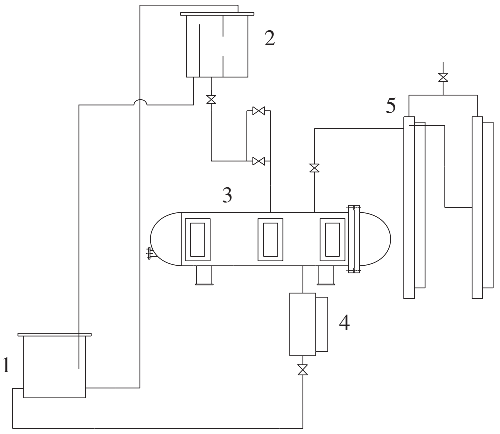

Fig. 1. Schematic of evaporation outside a horizontal tube. 1. Heating tank; 2. liquid feeder; 3. evaporator; meeting pot and 5. Condenser.

The test tube is made of HAL77–2A aluminum-brass with the outer diameter 25.4 mm, inner diameter 24 mm, and length 2,000 mm. Heat flux is provided by an electric heater embedded inside of the tube and the heat flux is ranging from 0 to 3 kW. Brine salinity varies from 30 to 70 g/kg. Evaporation temperature is from 50 to 70˚C and liquid flow rates from 0.026 to 0.09 kg/m s.

2.2. Experiment 2: Condensation inside a horizontal tube

This experiment aims at obtaining the condensation heat transfer and flow resistance when steam flows and condenses inside a horizontal tube. As shown in Fig. 2, the test facility consists of a boiler, a test tube divided into five sections, a vapor–liquid separator, two vapor condensers, a condensate tank, and a cooling water tank. The steam generated from the boiler enters the inside of the test tube where it is cooled by the cooling water outside the tube and condensed along the tube.

The test tube is made of HAL77–2A aluminum-brass with the outer diameter of 25.4 mm, inner diameter of 24 mm, and the length of 9,000 mm. For its five sections, every two of the adjacent tubes are connected by a quartz glass tube through which the flow pattern of two phase flow inside be observed.

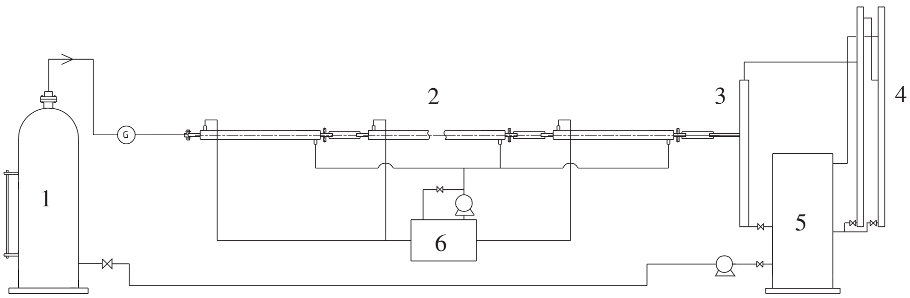

Fig. 2. Schematic sketch of condensation inside a horizontal tube.
1. Boiler; 2. testing part; 3. steam–liquid seperator; 4. condenser; 5. reservoir; 6. cooling water tank.

During experiments, steam temperature varies from 40 to 70℃, inlet steam velocity from 20 to 80 m/s, and inlet temperature difference from 4 to 8℃.

2.3. Experiment 3: Steam flow resistance across tube bundle

Intertube steam flow resistance across the tube bundle at different liquid flow densities and temperatures is measured in this experiment. As is shown in Fig. 3, the experimental setup is comprised of a boiler, a test section, a condenser, and a water tank. The steam generated from the boiler is sucked into the test section then passes horizontally across the tube bundle along its column direction, while water flowing downward outside tubes. The temperatures of the liquid and steam are equal. No heat exchange happens between the two phases. The steam is condensed at the condenser.

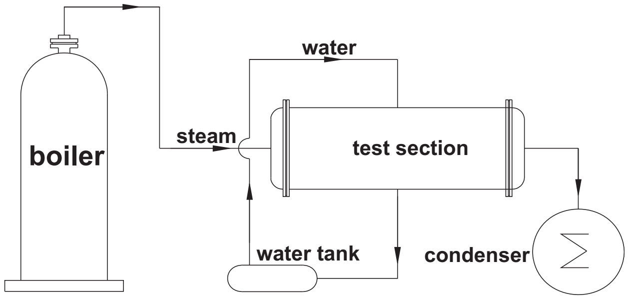

Fig. 3. Schematic sketch of steam flow resistance across tube bundle.

The tube bundle inside the test section is in the triangular arrangement. Steam velocity varies between 2 and 12 m/s, liquid flow density between 0.02 and 0.09 kg/m s, and steam temperature between 50 and 70℃.

3. Physical model

Fig. 4(a) shows the configuration of a large scale falling film evaporator. On the tube side, the steam flows and condenses along the tube length direction. On the shell side, the brine flows from the top row to the bottom row forming steady liquid films on the surface of the tubes. During this process, the brine

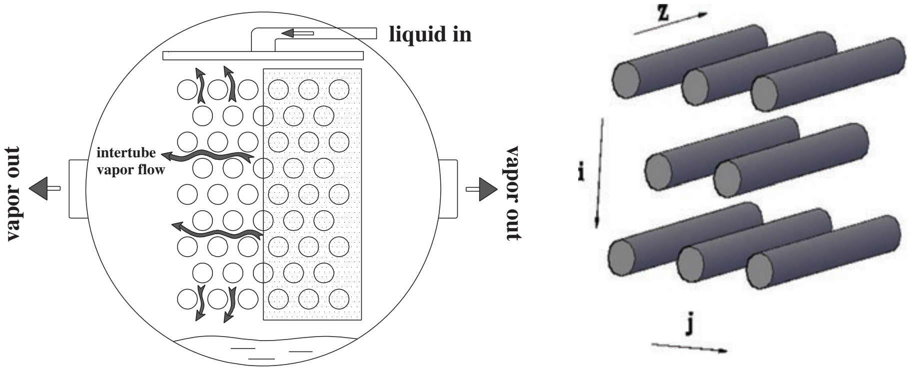

(a) Cross-section of the evaporator

(b) Three-dimensional grid generation

Fig. 4. Schematic of falling film evaporator and grid generation.

film is heated by the steam on the tube side and evaporates. The vapor detaches from the brine film and flows among tubes. Within the evaporator, along the tube row direction, the brine spray density and salinity change from top to bottom due to the continuous evaporation. The temperature of steam inside tubes varies along the tube length direction due to the steam pressure change. Besides, because of the flow resistance of the intertube vapor, the intertube vapor pressure and temperature change along its flow directions.

4. Mathematical model

The calculation of the falling film evaporator is based on the following assumptions:

(1) the evaporator is insulated from the surroundings;
(2) uniform distribution of brine film is achieved on the top row of the tube bundle at the saturated temperature; and
(3) effects of fouling resistance on heat transfer are neglected.

In order to reduce the calculation time, half the tube bundle is chosen as the calculation area considering its symmetric configuration in the horizontal direction and the identical heat transfer process for the two parts as shown in Fig. 4(a). The three-dimensional grid generation is demonstrated in Fig. 4(b). The grid points *i* and *j* are the tube row and column number, respectively. The grid point *z* denotes each discrete element along the tube length direction. The total grid number is 48,000 with the deviation in calculated heat flux no bigger than 0.02%.

Three modules are calculated, respectively, for each unit volume in the calculation area: the brine module, the inside-tube steam module, and the intertube vapor module.

4.1. The brine module on the shell side

The brine spray density Γ and salinity *S* yield the following equations:

$$\Gamma_{i,j,z} L_{i,j,z} = \Gamma_{i-1,j,z} L_{i-1,j,z} - m_{e,i-1,j,z} \tag{1}$$

$$S_{i,j,z} = S_{i-1,j,z} \Gamma_{i-1,j,z} / \Gamma_{i-1,j,z} \tag{2}$$

The heat transfer coefficient of brine falling film is determined through experiment 1:

$$\mathrm{Nu}_e = 0.0532\,\mathrm{Re}_{br}^{0.21}\,\mathrm{Pr}_{br}^{0.731} e^{-0.02283S} \tag{3}$$

where $\mathrm{Re}_{br} = 4\Gamma / \mu_{br}$.

The boundary conditions can be expressed as follows:

$$\Gamma_{i,j,z} = \Gamma_{inlet} \quad \text{for } j = 1, 2, \ldots, N_{col}, \; z = 1, 2, \ldots, N_{len}, \text{ at } i = 1 \tag{4}$$

$$S_{i,j,z} = S_{inlet} \quad \text{for } j = 1, 2, \ldots, N_{col}, \; z = 1, 2, \ldots, N_{len}, \text{at } i = 1 \tag{5}$$

$$\begin{aligned} T_{e,i,j,z} = T_{e,bd} \quad & \text{for } \; j = 1, 2, \ldots, N_j, \\ & z = 1, 2, \ldots, N_{len}, \;\text{ at }\; i = 1 \;\text{ and }\; i = 1, 2, \ldots, N_{row}, \\ & z = 1, 2, \ldots, N_z \;\text{ at }\; j = 1 \;\text{ and }\; j = 1, 2, \ldots, N_{len}, \\ & z = 1, 2, \ldots, N_{len}, \;\text{ at }\; i = N_{row} \end{aligned} \tag{6}$$

where Γ_{inlet}, S_{inlet} are the brine inlet spray density and inlet salinity, $T_{e,bd}$ is the vapor temperature at the boundary of the tube bundle. Within the range of $163.86 < \mathrm{Re}_{br} < 826.32$, $2.97 < \mathrm{Pr}_{br} < 4.13$ and $30\ \mathrm{g/kg} < S < 70\ \mathrm{g/kg}$, the prediction results of the correlation are in good agreement with the experiment data with the deviation of ±7.5%.

4.2. The tube-side steam module

The condensation heat transfer coefficient inside a tube is obtained from experiment 2:

$$h_c = 0.05775 \left[\frac{\rho_l (\rho_l - \rho_{st}) g \lambda_l^3 r}{\mu_l D_c \Delta T_c} \right]^{0.25} (-0.944x^2 + 0.841x + 0.291) \tag{7}$$

The steam pressure drop is also experimentally measured in experiment 2, and a valid equation was correlated as follows:

$$\Delta p_c = 11.2 \rho_{st}\, v_{st}^2 \mathrm{Re}_{st}^{-0.234} x^{5/3} \tag{8}$$

The calculation is along the tube length direction:

$$p_{c,i,j,z} = p_{c,i,j,z-1} - \Delta p_{c,i,j,z-1} \tag{9}$$

The boundary conditions are as follows:

$$T_{c,i,j,z} = T_{c,inlet} \quad \text{for } \; i = 1, 2, \ldots, N_{row}, \; j = 1, 2, \ldots, N_{len} \;\text{ at }\; z = 1 \tag{10}$$

$$\Delta p_{\mathrm{c,total,i,j}} = \Delta p_{\mathrm{c,total,1,1}} \quad \text{for} \quad i = 2,3,\ldots,N_{\mathrm{row}}, \quad j = 2,3,\ldots,N_{\mathrm{len}} \tag{11}$$

where $T_{\mathrm{c,inlet}}$ is the inlet steam temperature of tube bundle and $\Delta p_{\mathrm{c,total,1,1}}$ represents the total pressure drop between inlet and outlet of the first tube. Within the range of $\mathrm{Re}_{\mathrm{st}} < 30{,}000$, $20\ \mathrm{m/s} < v_{\mathrm{st}} < 80\ \mathrm{m/s}$, $0 < x < 1$ and $0.16\ \mathrm{kg/m^3} < \rho_{\mathrm{st}} < 0.65\ \mathrm{kg/m^3}$, Eq. (7) for predicting the condensation heat transfer coefficient and Eq. (8) for predicting the steam pressure drop are in agreement with the experiment data with the deviation of ±20%.

4.3. The intertube vapor module

Through experiment 3, the intertube vapor flow resistance was experimentally measured and correlated as the function of vapor flow rate and liquid flow density:

$$\Delta p_{\mathrm{e}} = \frac{1}{2\rho} N_{\mathrm{e}} G_{\mathrm{e}}^{2} \left(23.1 \mathrm{Re}_{\mathrm{e}}^{-1.1} \mathrm{Re}_{\mathrm{br}}^{0.926} + 4.07 \mathrm{Re}_{\mathrm{e}}^{-0.216}\right) \tag{12}$$

where $\mathrm{Re}_{\mathrm{e}} = \frac{u_{\mathrm{e}} \cdot D_{\mathrm{e}}}{v}$, $\mathrm{Re}_{\mathrm{br}} = 4\Gamma_{\mathrm{br}}/\mu_{\mathrm{br}}$, N_{e} represents the tube column number that the vapor has passed across, and G_{e} is the intertube vapor mass flow rate.

The calculation is along the tube column direction and row direction, respectively:

$$\begin{aligned} p_{\mathrm{e,i,j,z}} &= p_{\mathrm{e,i,j-1,z}} + \Delta p_{\mathrm{e,i,j-1,z}} \quad \text{or} \\ p_{\mathrm{e,i,j,z}} &= p_{\mathrm{e,i\pm1,j,z}} + \Delta p_{\mathrm{e,i\pm1,j,z}} \end{aligned} \tag{13}$$

depending on which direction has smaller flow resistance.

The boundary conditions are as follows:

$$\begin{aligned} p_{\mathrm{e,i,j,z}} = p_{\mathrm{e,inlet}} \quad &\text{for} \quad j = 1,2,\ldots,N_{\mathrm{j}}, \\ &z = 1,2,\ldots,N_{\mathrm{len}}, \quad \text{at} \quad i = 1 \quad \text{and} \quad i = 1,2,\ldots,N_{\mathrm{row}}, \\ &z = 1,2,\ldots,N_{\mathrm{z}} \quad \text{at} \quad j = 1 \quad \text{and} \quad j = 1,2,\ldots,N_{\mathrm{len}}, \\ &z = 1,2,\ldots,N_{\mathrm{len}}, \quad \text{at} \quad i = N_{\mathrm{row}} \end{aligned} \tag{14}$$

within the variation range of $0.19\ \mathrm{kg/m^2\,s} < G_{\mathrm{e}} < 1.1\ \mathrm{kg/m^2\,s}$, $204.41 < \mathrm{Re}_{\mathrm{e}} < 826.32$ and $0.16\ \mathrm{kg/m^3} < \mathrm{re} < 0.65\ \mathrm{kg/m^3}$, Eq. (12) is in agreement with the experimental date with the deviation of ±10%.

4.4. Governing equation

The heat flux for evaporation side equals to that on the condensation side:

$$h_{\mathrm{e,i,j,z}} A_{\mathrm{e,i,j,z}} \Delta T_{\mathrm{e,i,j,z}} = h_{\mathrm{c,i,j,z}} A_{\mathrm{c,i,j,z}} \Delta T_{\mathrm{c,i,j,z}} \tag{15}$$

5. Algorithm

The algorithm of the model is shown in Fig. 5. The total steam pressure drop of the first tube $\Delta p_{\mathrm{c,total,1,1}}$ is calculated at the very beginning as $\Delta p_{\mathrm{c,total,initial}}$ and it serves as a boundary condition for the calculation of the rest of tubes which is illustrated in Eq. (11). For every unit volume, the values of three modules are updated in each loop. The initial hypothetical values are modified until the convergence of all parameters is reached.

6. Results and discussions

6.1. The distribution of the local brine spray density Γ and the local salinity S

The distributions of Γ and *S* are illustrated in Figs. 6 and 7, respectively. Due to the continuous evaporation of the brine, Γ decreases along the tube row direction as depicted in Fig. 6. *S* increases along the tube row direction as shown in Fig. 7. Compared

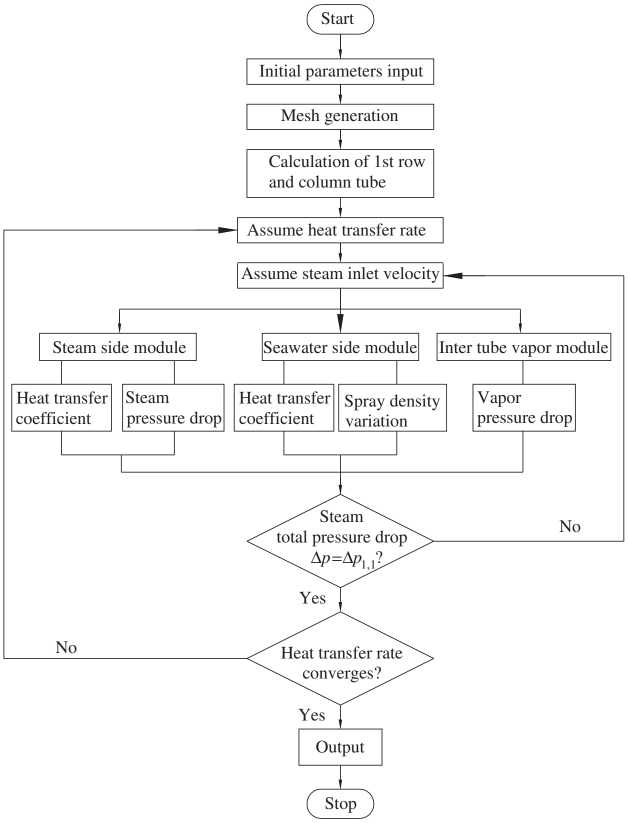

Fig. 5. Flowchart of the numerical algorithm.

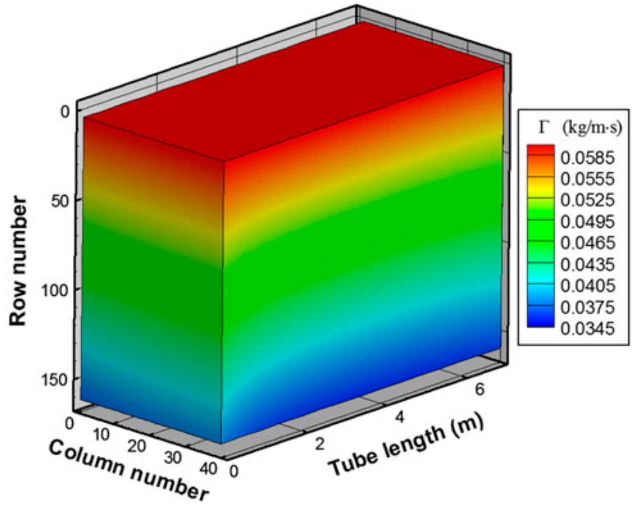

Fig. 6. The distribution of the brine local spray density.

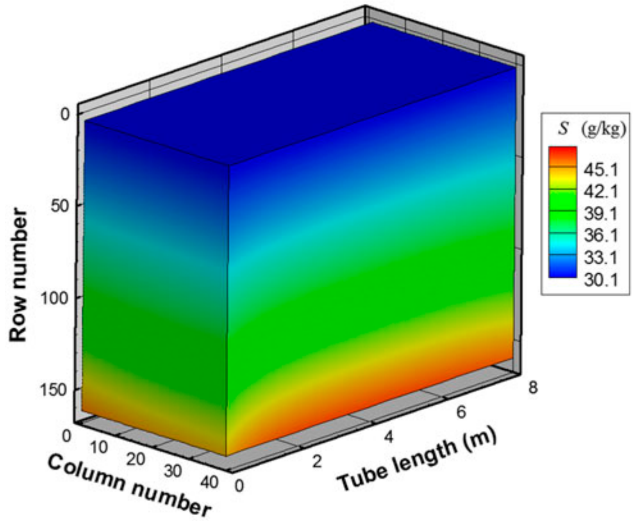

Fig. 7. The distribution of the brine local salinity.

with these two figures, it is noted that the variations of Γ and S are mainly along the brine flow direction which is the tube row direction. Along this direction, Γ decreases by 42.63% and correspondingly the brine salinity increases by 42.63%. Γ also shows slight variation along the tube length direction and the column direction due to the difference in the heat flux at different locations. Where it has higher heat flux, Γ has smaller values. From Fig. 6, it is noted that along the tube length direction, Γ has relative lower values near the center of the tube than near the two ends due to the larger heat transfer in this area. Along the tube column direction, similarly due to non-uniform distribution of heat flux, Γ has relative lower values near the boundary than near the center of the bundle.

6.2. The distribution of the intertube vapor velocity v_e

The distribution of the intertube vapor velocity, v_e, is shown in Fig. 8. The tube bundle is divided into three zones according to the flow direction of the intertube vapor: the upper zone, the middle zone, and the lower zone. In the upper zone, the intertube vapor mainly flows vertically upwards toward the top row. In the center zone, vapor mainly flows horizontally toward the boundary of the tube bundle. Similarly, for the lower zone, the intertube vapor flows mainly downwards toward the bottom row. The flow direction of the intertube vapor is determined by the vapor flow resistance to the edge of the tube bundle. The intertube vapor always flows along the direction that has smaller flow resistance. Fig. 8 shows that the velocity gradient of the intertube vapor depends on the zones. The upper and lower zones have relatively lager velocity gradient than the center zone along the vapor flow directions. It has close relation with the tube arrangement. It can be seen in Fig. 9 that for the triangular tube bundle arrangement, the intertube vapor has a larger flow area when it flows horizontally than flowing vertically. For the upper and lower zones, the vertical flows have larger flow areas compared to that of the center zone. Consequently, the vapor has larger velocity gradients in these two zones than in the center zone. The simulation results show that the maximal value of v_e in the vertical direction is 11.57 m/s, while for the horizontal direction, it is 5.89 m/s.

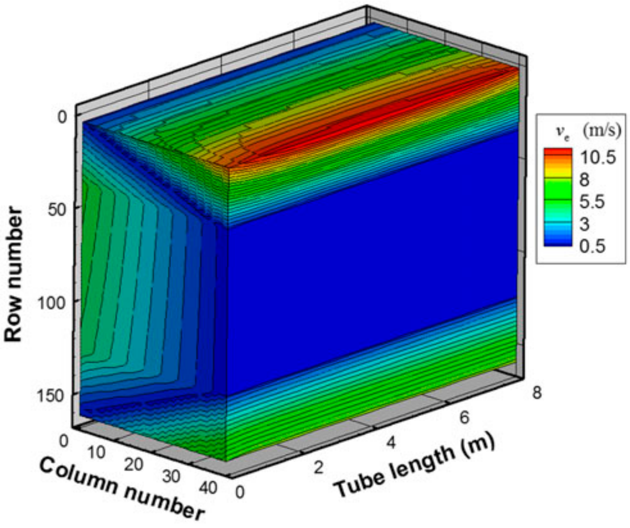

Fig. 8. The distribution of the intertube vapor velocity.

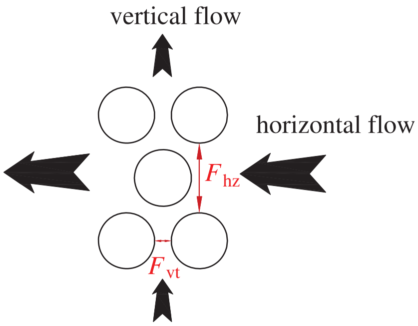

Fig. 9. Schematic of the flow area of the intertube vapor.

It is also noted in Fig. 8 that the center zone accounts for the larger part of the tube bundle. The simulation results show that the center part covers 78% of the volume of the tube bundle which means that for the larger part of the tube bundle, the intertube vapor flows horizontally to the boundary of the tube other than flowing vertically to the boundary. It is because that for most part of the tube bundle, the vapor has smaller flow resistance when flows horizontally than vertically. Besides, within the center zone, upper tubes are found to have larger vapor velocity gradient than lower tubes along tube column direction. It is caused by the decrease of Γ. On the one hand, the decreases of Γ from upper tubes to lower ones enlarges the flow space of the intertube vapor among tubes, which leads to smaller vapor velocity gradient along the tube column direction. On the other hand, lower tubes have smaller heat flux due to the decrease in the local heat transfer coefficient, which is caused by the decrease of Γ as well as the increase of *S*. Less vapor is generated among lower tubes causing smaller vapor velocity gradients along column direction for lower tubes than upper tubes for the center zone.

6.3. The distribution of the intertube vapor pressure p_e and temperature T_e

Along the tube row and column directions, it can be seen in Fig. 10 that at the boundary of the tube bundle, the intertube vapor pressure, p_e, has the smallest value. For all the zones, p_e decreases along the vapor flow directions due to the vapor flow resistance. For the upper zone and the lower zone, the intertube vapor has relative larger velocity gradient along the flow direction as introduced in the above section. In consequence, the intertube vapor has relatively larger pressure gradients in the upper zone and the lower zone than in the center zone along the vapor flow directions.

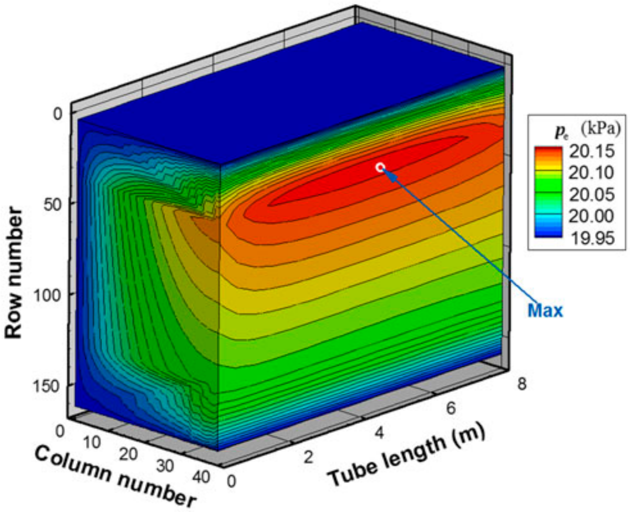

Fig. 10. The distribution of the vapor pressure on the shell side.

Along the tube length direction, p_e increases slightly followed by a slight decrease. It is due to the non-uniform distribution of heat flux along the tube length direction. Along this direction, relatively more vapor is generated at the center of the tube than the two ends. In this case, the intertube vapor has relatively larger flow resistance near the center part than near the two ends of the tubes when it flows horizontally across the tubes. p_e thus has relatively higher values near the center of the tubes than at the two sides.

The maximum of p_e is located at the upper zone which reaches 20.15 kPa compared to the minimum value which is 19.95 kPa as shown in Fig. 10. The calculation results show that the maximum saturated temperature variation caused by the vapor flow resistance is 0.22℃ which accounts for 7.3% of the superficial overall temperature difference which is 3℃ in this paper.

Fig. 11 demonstrates the distribution of T_e. It can be seen that the distribution law of vapor temperature is not in accord with the vapor pressure in Fig. 10. This is due to the boiling point elevation, BPE, of the brine. According to Sharqawy et al. [18], BPE changes with the variation of the temperature and the salinity of the brine. Within the evaporator, the main parameter that affects the value of BPE is the brine salinity considering the variation range of brine temperature is too small. The distribution of BPE is displayed in Fig. 12. It coincides well with the distribution of the local brine salinity as depicted in Fig. 7. Along the tube row direction, BPE increases due to the increment of *S*. The maximum variation of T_e caused by the variation of BPE is 0.22℃ which accounts for 7.3%

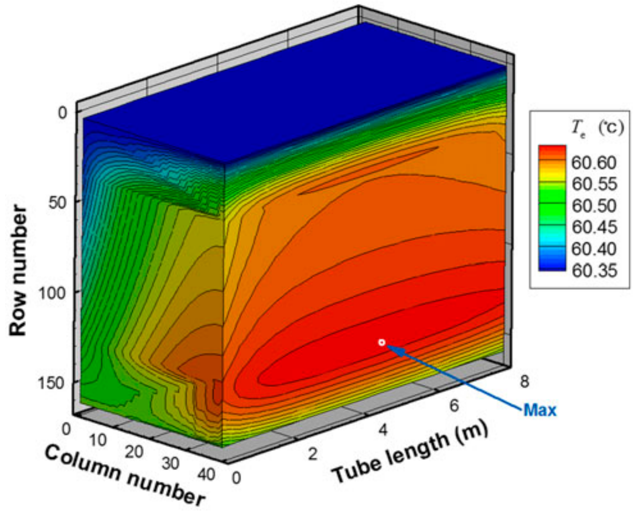

Fig. 11. The distribution of the vapor temperature on the shell side.

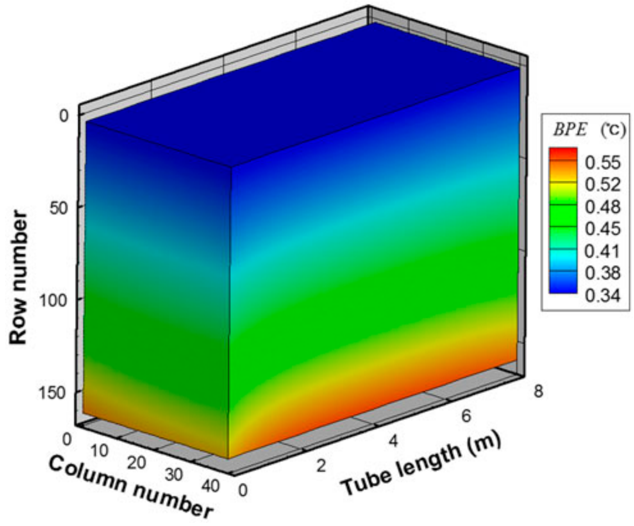

Fig. 12. The distribution of the boiling point elevation.

of the superficial overall temperature difference which is 3℃. The distribution of T_e is affected by both the influence of the vapor flow resistance and the variation of BPE. It can be seen from Fig. 11 that the top row of the tube bundle has the smallest T_e where the vapor has the smallest pressure and the brine has the smallest BPE. The maximum value of T_e is located at the boundary of the center zone and the lower zone where the vapor has relative high pressure and the brine has relative larger value of BPE. Under the operating condition of this paper, the maximum vapor temperature variation is 0.3℃ which accounts for 10.0% of the superficial overall temperature difference. Taking into account, the intertube vapor temperature variation is of significant importance for the design of large falling film evaporators.

6.4. The distribution of the condensation temperature T_c

The distribution of T_c inside the tube is illustrated in Fig. 13. It is indicated that T_c mainly varies along the tube length direction. For all the tubes, the steam enters the inlets of the tubes at the same temperature. Because the tube bundle is connected by the headers at each end, all the tubes have the same total pressure drop. So the steam leaves the outlets also with the same pressure and temperature. It can be seen from Fig. 13 that for all the tubes, T_c decreases more rapidly near the steam inlets than near the steam outlets. It is due to the higher steam velocities near the inlets than near the outlets. Since T_c has the same temperature drop between the inlets and the outlets for all the tubes, it is also shown in Fig. 13 that near the steam inlets, T_c decreases more rapidly for the upper rows than the lower; near the steam outlets, T_c decreases faster for the lower tubes than the upper. It is due to the non-uniform distribution of the steam inlet velocity among tubes. For the falling film evaporator that has a tube bundle connected by the headers, all the heat transfer tubes have the same steam total pressure drop. The tubes that have larger heat flux absorb more steam to maintain the pressure balance [19]. As depicted in Fig. 14, the upper tubes have higher steam inlet velocities than lower tubes because they have larger heat flux. The higher steam inlet velocities for

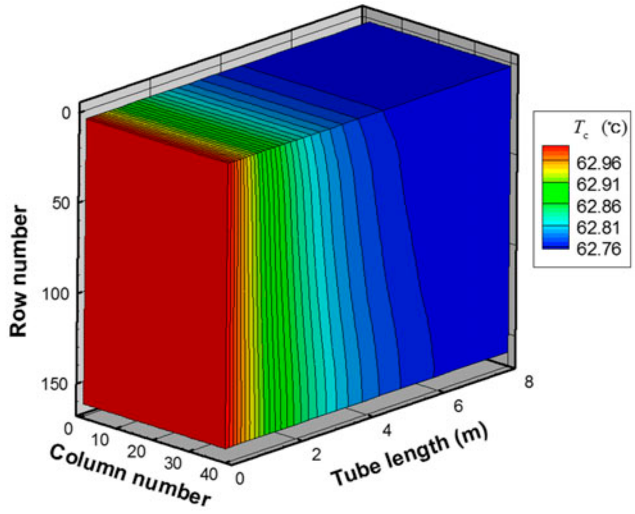

Fig. 13. The distribution of the condensation temperature.

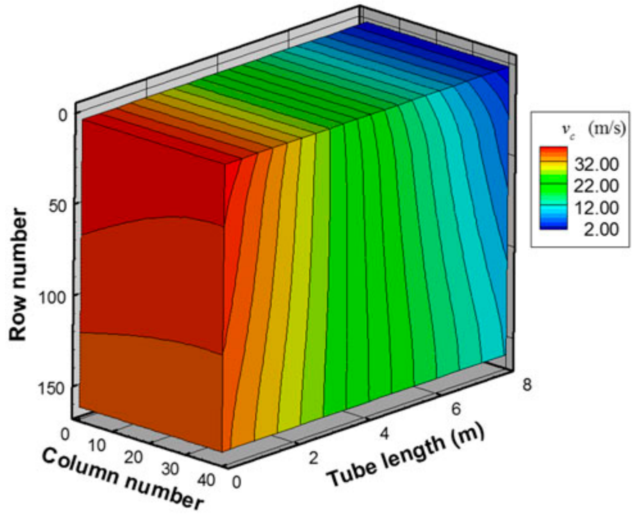

Fig. 14. The distribution of the steam local velocity.

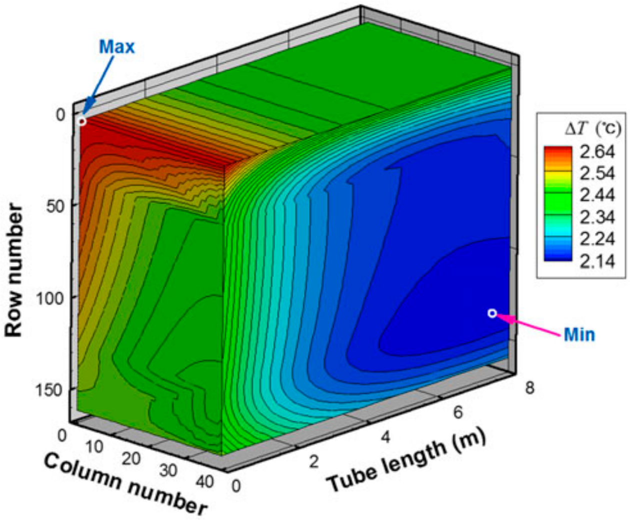

Fig. 15. The distribution of the overall temperature difference.

upper tubes lead to larger steam flow resistance. Thus, near the steam inlets, the steam has larger pressure drop and consequently larger temperature drop for the upper tubes than the lower tubes. It is also because that the upper tubes have larger heat flux, the steam velocity decreases more rapidly for the upper tubes than the lower tubes. Near the steam outlets, the upper tubes have smaller velocities than the lower tubes as shown in Fig. 14. In consequence, T_c drops more slowly for upper tubes than lower tubes when the steam is near to the outlets.

6.5. The distribution of the local overall temperature difference ΔT

Along the tube column number and row number directions, the distributions of ΔT are mainly determined by the distributions of the intertube vapor temperature. As is shown in Fig. 15, ΔT decreases along the vapor flow directions because T_e is increasing along this direction as displayed in Fig. 11. The maximum ΔT is 2.66℃ and is located at the top row. It is because of the existence of BPE that the maximum ΔT is less than the superficial overall temperature difference which is 3℃. The minimum value of ΔT is marked in Fig. 15 which is 2.12℃. It is located at the boundary of the upper zone and the center zone and is near to the steam outlet. At this point, T_e has a relative high value and T_c has a relative small value.

Along the tube length direction, ΔT firstly decreases rapidly and increases slightly after. The rapid decrease of ΔT near the steam inlet is due to the decrease of T_c along the tube length direction as shown in Fig. 13. The sight increase of ΔT near the steam outlet is because of the slight decrease of T_e near the steam outlet as shown in Fig. 11.

6.6. The distribution of the heat transfer coefficient *h* and the heat flux *q*

It can be seen from Fig. 16 that *h* is non-uniformly distributed in the evaporator. It exhibits more significant variation range along the tube row direction and the tube length directions than along the tube column direction. *h* has the maximum value near the center part of the top row tubes. The minimum value of *h* is located at the steam inlet for the bottom row tubes.

Along the tube length direction, *h* increases to the maximum value firstly and then decreases as shown in Fig. 16. This phenomenon is mainly caused by the heat transfer performance inside the tubes [20]. In the experiment 2, the steam generated from the boiler with a relative low velocity is sucked into the inlet of tube inside at a relative high velocity. This procedure covers a very short distance of the test section and could be regarded as an isenthalpic process. Steam at the forepart of the tube then has a certain degree of superheat. Stable condensation film could hardly be formed, thus the heat transfer coefficient on the tube side has relatively lower values near the steam inlets. As the steam continuously flows along the tube direction, the film condensation gradually dominates the heat transfer process. *h* then gradually increases. When steam further flows toward the outlets, the condensate gradually accumulates at the bottom of tubes, *h* thus gradually decreases.

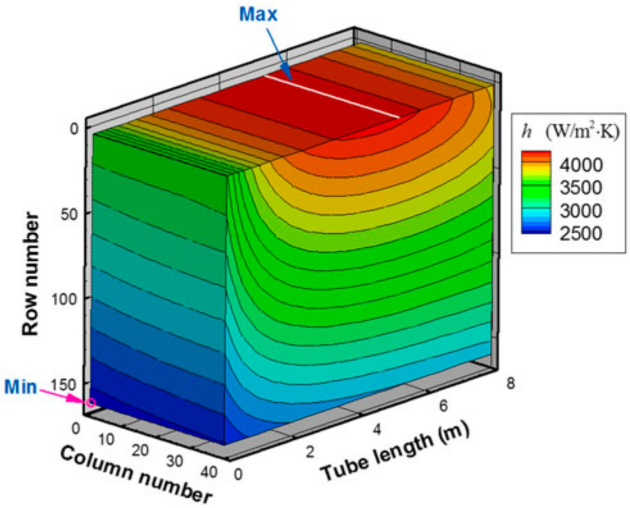

Fig. 16. The distribution of the heat transfer coefficient.

Along the tube row direction, h shows a decreasing trend. This phenomenon is accord to the conclusion drawn by Zeng et al. [21] that upper tubes in a tube bundle have better heat transfer performance than the lower tubes. On the one hand, the decrease of brine spray density leads to weaker film turbulence outside tube surfaces. On the other hand, the increase of brine salinity causes the increase in the brine viscosity and surface tension. Both are unfavorable to the heat transfer performance on the evaporation side. In consequence, h exhibits a decreasing trend with the increase of the tube row number.

Along the tube column direction, to better display the variation of h, Fig. 17 is given to demonstrate the averaged heat transfer coefficient, $\bar{h}$, along the tube row and column directions. It is noted that $\bar{h}$ increases with the increase of tube column number. Along this direction, $\bar{h}$ is found to increase by 1.69% on average. The increase of $\bar{h}$ along the tube column direction results from the decrease of ΔT along this direction as shown in Fig. 15. The decrease of ΔT leads to the decrease of the heat flux and consequently the increase of brine spray density and the decrease of brine salinity along the tube column direction. Both are favorable for the heat transfer performance on the shell side. Besides, the decrease of the heat flux along this direction lead to thinner condensation film and lower condensate level on the tube side. It also leads to increases of $\bar{h}$ along the tube column direction.

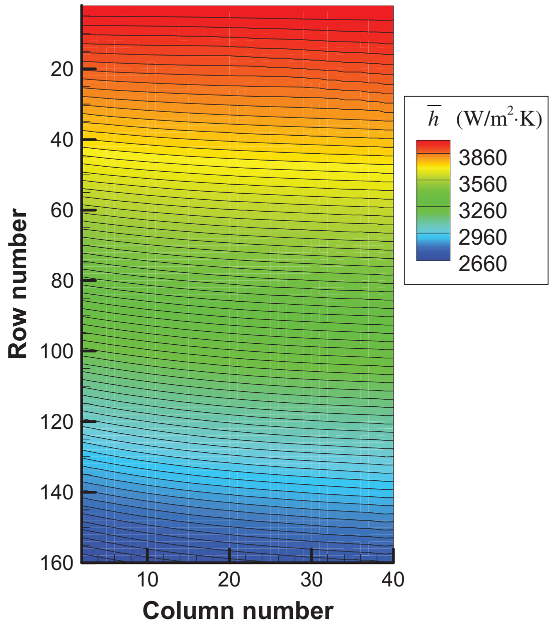

Fig. 17. The distribution of the averaged heat transfer coefficient in the tube row–column plane.

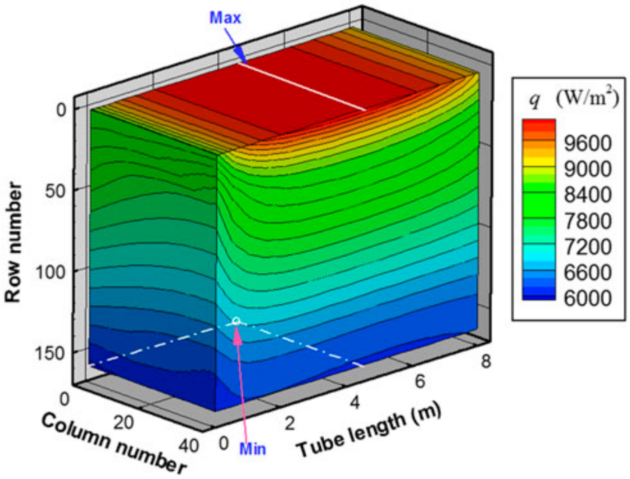

Fig. 18. The distribution of the heat flux.

The distribution of q is displayed in Fig. 18. It is noted that the distribution of h dominants the distribution of q along the tube length direction, so q shows an increasing trend for the forepart of the tube followed by a slight decreasing trend after. Along the tube row direction, q shows a rapid decreasing trend. It is due to both the decrease of h and ΔT along this direction. The maximum of q is located at the center part of the top row tubes where h also has the maximum values. The minimum of q is located at the center part of the bottom row tube where both h and ΔT have relatively smaller values.

To better illustrate q along the tube column direction, the averaged heat flux, $\bar{q}$, along the tube row and

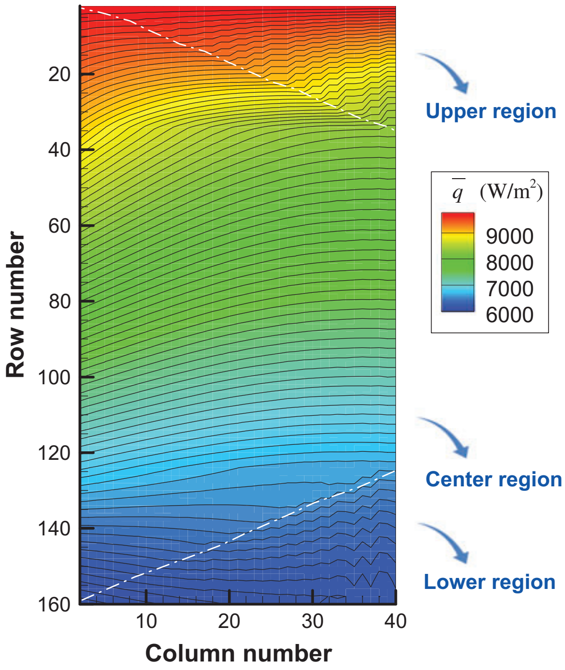

Fig. 19. The distribution of the averaged heat flux in the tube row–column plane.

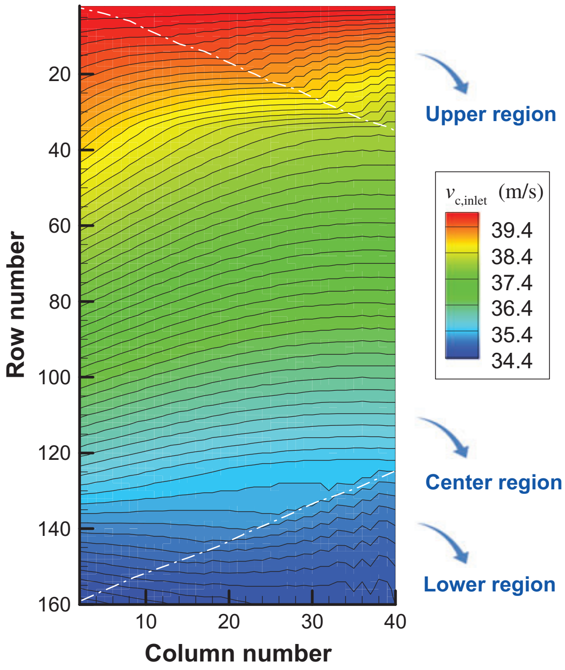

Fig. 20. The distribution of steam inlet velocity.

column directions is displayed in Fig. 19. It can be seen that the distribution of $\bar{q}$ has close relation with the intertube vapor flow direction. Within the three zones, $\bar{q}$ increases along the intertube vapor flow directions mainly because ΔT is increasing along this direction as shown in Fig. 15.

6.7. The distribution of the steam inlet velocity $v_{c,inlet}$

As illustrated in the above section, the heat flux varies from tube to tube. For all the tubes, their steam fore and aft pressure drops are of the same value. Assuming that all the tubes share the same $v_{c,inlet}$, the total steam pressure drop must vary from tube to tube. The tubes that have smaller heat flux must have relative higher average velocities and consequently larger total pressure drops. In fact, the tubers with larger heat flux absorb more steam into the tubes to keep the pressure balance. The non-uniform distribution of $v_{c,inlet}$ is shown in Fig. 20. It can be seen that the distribution of $v_{c,inlet}$ well coincides with the distribution of $\bar{q}$ in the tube row–column plane as displayed in Fig. 19. Under the operating condition of this paper, the maximum $v_{c,inlet}$ is of 40 m/s, while the minimum is 34.3 m/s.

7. Concluding remarks

A comprehensive model has been developed based on three experiments to predict the performance in a large falling film horizontal-tube bundle evaporator. Parameters on both the evaporation side and the condensation side have non-uniform distributions along the three directions. The results suggest the following conclusions:

1. The brine spray density and salinity mainly vary along the tube row direction due to the evaporation of the brine. Along the tube length direction, the spray density and salinity also show slight variation due to the non-uniform distribution of heat flux.
2. In the tube bundle, the horizontal intertube vapor covers more volume of the tube bundle than the vertical flow. Along the horizontal direction, the intertube vapor has relative smaller velocity gradient than along the vertical direction.
3. Along the tube row and column directions, the distribution of the overall temperature difference is mainly determined by the intertube vapor temperature.

(4) The heat transfer coefficient has a larger variation range along the tube length and tube row directions than along the tube column direction. The maximum heat transfer coefficient exists at the center part of tubes for the top row. The minimum heat transfer coefficient is located at the steam inlet of the bottom row.

(5) Due to the variation of heat transfer performances, steam enters the inside of tubes at different velocities to maintain the pressure balance. The distribution of steam inlet velocity is mainly determined by the distribution of the heat flux.

Acknowledgments

The authors are grateful for the support of the Key Project of the National Natural Science Foundation of China (No. 51336001) and the Research Fund for the Doctorial Program of Chinese Universities (20110041110032).

Nomenclature

A — heat transfer area, m^2
D — diameter of tube, m
F_{Hz} — flow area for horizontal flow of intertube vapor
F_{vt} — flow area for vertical flow of intertube vapor
g — gravitational acceleration, m/s^2
h — heat transfer coefficient, W/m^2 K
L — tube length, m
m — mass flow rate, kg/s
N — grid number
N_{e} — tube column number that the intertube vapor has passed across
N_{row} — total grid number along the tube row direction
N_{col} — total grid number along the tube column direction
N_{len} — total grid number along the tube length direction
Nu — nusselt number
Pr — prandtl number
p — pressure, Pa
Δp — pressure drop, Pa
$\Delta p_{\mathrm{total}}$ — steam total pressure drop between inlet and outlet, Pa
q — heat flux, kW/m^2
r — latent heat, J/kg
Re — reynolds number
S — brine salinity, g/kg
T — temperature, ℃
ΔT — local temperature difference, ℃
$v_{\mathrm{c,inlet}}$ — tube-side steam inlet velocity, m/s
v_{e} — intertube vapor velocity, m/s
v_{st} — tube-side steam local velocity, m/s
x — vapor quality
row, col, len — space coordinates along the tube row, column, and length directions

Greeks symbols

Γ — local brine spray density, kg/m s
λ — thermal conductivity, W/m K
μ — dynamic viscosity, N s/m^2
ρ — density, kg/m^3
v — kinematic viscosity, m^2/s

Subscripts

bd — parameters at the boundary of the tube bundle
br — brine on the evaporation side
c — the condensation side
e — evaporation side/vapor on the evaporation side
i — grid number along the tube row direction
inlet — parameters at the inlets
j — grid number along the tube column direction
l — liquid on the condensation side
outlet — parameters at the outlets
st — steam on the condensation side
z — grid number along the tube length direction

References

[1] L.S. Fletcher, V. Sernas, L.S. Galowin, Evaporation from thin water films on horizontal tubes, Ind. Eng. Chem. Process. Des. Dev. 13 (1974) 265–269.

[2] L.S. Fletcher, V. Sernas, W.H. Parken, Evaporation heat transfer coefficients for thin sea water films on horizontal tubes, Ind. Eng. Chem. Process. Des. Dev. 14 (1975) 411–416.

[3] L. Yang, S. Shen, Experimental study of falling film evaporation heat transfer outside horizontal tubes, Desalination 220 (2008) 654–660.

[4] W.H. Parken, L.S. Fletcher, J.C. Han, V. Sernas, Heat transfer through falling film evaporation and boiling on horizontal tubes, J. Heat Transfer 112 (1990) 744–750.

[5] M.-C. Chyu, A. Bergles, An analytical and experimental study of falling-film evaporation on a horizontal tube, J. Heat Transfer 109 (1987) 983–990.

[6] J.W. Coleman, S. Garimella, Two-phase flow regimes in round, square and rectangular tubes during condensation of refrigerant R134a, Int. J. Refrig 26 (2003) 117–128.

[7] A. Cavallini, G. Censi, D. Del Col, L. Doretti, G.A. Longo, L. Rossetto, C. Zilio, Condensation inside and

outside smooth and enhanced tubes—A review of recent research, Int. J. Refrig 26 (2003) 373–392.

[8] J. El Hajal, J.R. Thome, A. Cavallini, Condensation in horizontal tubes, part 1: Two-phase flow pattern map, Int. J. Heat Mass Transfer 46 (2003) 3349–3363.

[9] J.R. Thome, J. El Hajal, A. Cavallini, Condensation in horizontal tubes, part 2: New heat transfer model based on flow regimes, Int. J. Heat Mass Transfer 46 (2003) 3365–3387.

[10] P.A. Berthelsen, T. Ytrehus, Calculations of stratified wavy two-phase flow in pipes, Int. J. Multiphase Flow 31 (2005) 571–592.

[11] S. Shen, R. Liu, Y. Yang, X. Liu, J. Chen, Condensation character of a stratified flow inside a horizontal tube, Desalin. Water Treat. 33 (2011) 218–223.

[12] L. Xu, M. Ge, S. Wang, Y. Wang, Heat-transfer film coefficients of falling film horizontal tube evaporators, Desalination 166 (2004) 223–230.

[13] Z.-H. Liu, Q.-Z. Zhu, Y.-M. Chen, Evaporation heat transfer of falling water film on a horizontal tube bundle, Heat Transfer—Asian Res. 31 (2002) 42–55.

[14] Y. Fujita, M. Tsutsui, Experimental investigation of falling film evaporation on horizontal tubes, Heat Transfer—Japanese Res. 27 (1998) 609–618.

[15] L. Yang, W. Wang, The heat transfer performance of horizontal tube bundles in large falling film evaporators, Int. J. Refrig 34 (2011) 303–316.

[16] H. Hou, Q. Bi, X. Zhang, Numerical simulation and performance analysis of horizontal-tube falling-film evaporators in seawater desalination, Int. Commun. Heat Mass Transfer 39 (2012) 46–51.

[17] S. Shen, G. Liang, Y. Guo, R. Liu, X. Mu, Heat transfer performance and bundle-depth effect in horizontal-tube falling film evaporators, Desalin. Water Treat. 51 (2013) 830–836.

[18] M.H. Sharqawy, J.H. Lienhard, S.M. Zubair, Thermophysical properties of seawater: A review of existing correlations and data, Desalin. Water Treat. 16 (2010) 354–380.

[19] S.Q. Shen, L.Y. Gong, H. Liu, et al., Characteristic study of steam maldistribution in horizontal-tube falling film evaporators, Appl. Therm. Eng. 75 (2015) 635–647.

[20] L. Gong, S. Shen, H. Liu, X. Mu, X. Chen, Three-dimensional heat transfer coefficient distributions in a large horizontal-tube falling film evaporator, Desalination 357 (2015) 104–116.

[21] X. Zeng, M.C. Chyu, Z.H. Ayub, Experimental investigation on ammonia spray evaporator with triangular-pitch plain-tube bundle, Part I: Tube bundle effect, Int. J. Heat Mass Transfer 44 (2001) 2299–2310.